Raman scattering through a metal-insulator transition

J. K. Freericks[1] and T. P. Devereaux[2]
[1]*Department of Physics, Georgetown University, Washington, DC 20057*
[2]*Department of Physics, University of Waterloo, Waterloo, Ontario, Canada N2G 1Y2*
(Received 3 April 2001; published 10 September 2001)

The exact solution for nonresonant A_{1g} and B_{1g} Raman scattering is presented for the simplest model that has a correlated metal-insulator transition, the Falicov-Kimball model, by employing dynamical mean-field theory. In the general case, the A_{1g} response includes nonresonant, resonant, and mixed contributions, and the B_{1g} response includes nonresonant and resonant contributions (we prove the Shastry-Shraiman relation for the nonresonant B_{1g} response), while the B_{2g} response is purely resonant. Three main features are seen in the nonresonant B_{1g} channel: (i) the rapid appearance of low-energy spectral weight at the expense of higher-energy weight; (b) the frequency range for this low-energy spectral weight is much larger than the onset temperature, where the response first appears; and (iii) the occurrence of an isosbestic point, which is a characteristic frequency where the Raman response is independent of temperature for low temperatures. Vertex corrections renormalize away all of these anomalous features in the nonresonant A_{1g} channel. The calculated results compare favorably to the Raman response of a number of correlated systems on the insulating side of the quantum-critical point (ranging from Kondo insulators to mixed-valence materials to underdoped high-temperature superconductors). We also show why the nonresonant B_{1g} Raman response is ''universal'' on the insulating side of the metal-insulator transition.

DOI: 10.1103/PhysRevB.64.125110 PACS number(s): 71.30.+h, 78.30.−j, 74.72.−h, 75.20.Hr

I. INTRODUCTION

Raman scattering has been an important experimental tool for studying lattice dynamics for over four decades (since the advent of the laser). More recently, it has been applied to study the scattering of electrons in metals, insulators, semiconductors, and superconductors. Via light's coupling to the electron's charge, inelastic light scattering reveals symmetry selective properties of the electron dynamics over a wide range of energy scales and temperatures. It is similar to the optical conductivity, which involves elastic scattering of light by electron-hole pairs, but Raman scattering provides additional information, since it is able to isolate different symmetry channels by selectively polarizing the incident light and measuring the reflected light with a polarized detector. Three principle symmetries are usually examined: (i) A_{1g}, which has the full symmetry of the lattice (i.e., is *s* like); (ii) B_{1g}, which is a *d*-like symmetry (which probes the Brillouin-zone axes); and (iii) B_{2g}, which is another *d*-like symmetry (which probes the Brillouin-zone diagonals). In 1990–1991, Shastry and Shraiman proposed a simple relation[1] that connects the nonresonant Raman response to the optical conductivity. We prove the Shastry-Shraiman relation here for the B_{1g} channel in the large-dimensional limit.

Strongly correlated systems as disparate as mixed-valence compounds[2] (such as SmB_6), Kondo insulators[3] (such as FeSi), and the underdoped cuprate high-temperature superconductors[4–6] show temperature-dependent B_{1g} Raman spectra that are both remarkably similar and quite anomalous. This ''universality'' suggests that there is a common mechanism governing the electronic transport in correlated insulators. As these materials are cooled, they all show a pileup of spectral weight for moderate photon energy losses with a simultaneous reduction of the low-frequency spectral weight. This spectral weight transfer is slow at high temperatures and then rapidly increases as the temperature is lowered towards a putative quantum-critical point (corresponding to a metal-insulator transition). In addition, the Raman spectral range is divided into two regions: one where the response decreases as T is lowered and one where the response increases. These regions are separated by a so-called isosbestic point, which is defined to be the characteristic frequency where the Raman response is independent of temperature. Finally, it is often observed that the range of frequency where the Raman response is reduced as T is lowered is an order of magnitude (or more) larger than the temperature at which the low-frequency spectral weight disappears. These anomalous features are not typically seen in either the A_{1g} or the B_{2g} channels.

Theory has lagged behind experiment for electronic Raman scattering in strongly correlated materials. While theories that describe Raman scattering in weakly correlated (Fermi-liquid) metals[7] or in band insulators[8] have been known for some time, it is only recently that a theory that describes materials near the metal-insulator transition has been developed.[9] This theoretical treatment involves applying the dynamical mean-field theory to the simplest many-body system that has a quantum-critical point—the spinless Falicov-Kimball model.[10] We choose this model as our canonical model for Raman scattering because it can be solved exactly and the results are universal for the nonresonant B_{1g} channel on the insulating side of the transition (we do not choose it because we believe that the Falicov-Kimball model is the physically relevant model for all correlated experimental systems—it is not). Other work has been performed in the so-called iterated-perturbation-theory approximation to the Hubbard model, where the nonresonant B_{1g} Raman response is determined.[11]

The Hamiltonian contains two types of electrons: itinerant band electrons and localized (d or f) electrons. The band

electrons can hop between nearest neighbors [with hopping integral $t^*/(2\sqrt{d})$ on a d-dimensional cubic lattice[12]], and they interact via a screened Coulomb interaction with the localized electrons (which is described by an interaction strength U between electrons that are located at the same lattice site). All energies are measured in units of t^*. The Hamiltonian is

$$H=-\frac{t^*}{2\sqrt{d}}\sum_{\langle i,j\rangle} d_i^\dagger d_j+E_f\sum_i w_i-\mu\sum_i (d_i^\dagger d_i+w_i) + U\sum_i d_i^\dagger d_i w_i, \tag{1}$$

where $d_i^\dagger$ (d_i) is the spinless conduction electron creation (annihilation) operator at lattice site i and $w_i=0$ or 1 is a classical variable corresponding to the localized f-electron number at site i. We will adjust both E_f and μ so that the average filling of the d electrons is 1/2 and the average filling of the f electrons is 1/2 ($\mu=U/2$ and $E_f=0$).

In this contribution we will show how to derive the nonresonant, mixed, and resonant Raman response of a system that crosses through a metal-insulator transition by solving the problem exactly in the large-dimensional limit (employing dynamical mean-field theory). In the case of nearest-neighbor hopping on a hypercubic lattice in infinite dimensions, we show that the A_{1g} response includes contributions from all processes, the B_{1g} response is resonant or nonresonant, and the B_{2g} response is purely resonant. We provide computational results only for the nonresonant A_{1g} and B_{1g} responses. Resonant (and mixed) Raman scattering results will be presented elsewhere. We also prove the Shastry-Shraiman relation, motivate the origin of the anomalous features in the nonresonant B_{1g} response, and show why they are not seen in the nonresonant A_{1g} channel.

We present the formalism in Sec. II which includes a detailed analysis of the Raman response in the different symmetry channels. In Sec. III we present the results of our calculations which display anomalous behavior for B_{1g} and ordinary behavior for A_{1g}. Our conclusions are presented in Sec. IV.

II. FORMALISM

A. Nonresonant Raman response

The Feynman diagrams for the nonresonant Raman response are shown in Fig. 1. The straight lines denote the momentum-dependent Green's function and the wavy lines denote the photon propagator. The shading is used to represent the renormalized susceptibility and the symbol Γ denotes the local irreducible charge vertex. The functions $\gamma(\mathbf{k})$ are called the Raman scattering amplitudes, and they are chosen to have a well-defined spatial symmetry and no frequency dependence. The Raman response is found from this frequency-dependent density-density correlation function which is

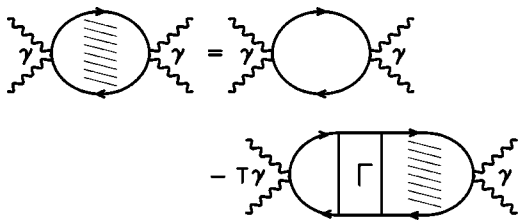

FIG. 1. Dyson equation for the nonresonant Raman response function. Solid lines denote electron propagators and wavy lines denote photon propagators. The shading denotes the fully renormalized susceptibility and the symbol Γ is the irreducible frequency-dependent charge vertex. The vertex function γ is the Raman scattering amplitude, which determines the symmetry of the Raman scattering channel.

$$\chi_{\rm Raman}(i\nu_l)=\sum_{\mathbf{k}}\int_0^\beta d\tau e^{i\nu_l\tau}\left\{\frac{{\rm Tr}\,T_\tau\langle e^{-\beta H}\rho_{\mathbf{k}}(\tau)\rho_{\mathbf{k}}(0)\rangle}{Z} -\left[\frac{{\rm Tr}\langle e^{-\beta H}\rho_{\mathbf{k}}(0)\rangle}{Z}\right]^2\right\}, \tag{2}$$

with the uniform $(\mathbf{q}=0)$ Raman density operator

$$\rho_{\mathbf{k}}=\gamma(\mathbf{k})d_{\mathbf{k}}^\dagger d_{\mathbf{k}}, \quad d_{\mathbf{k}}=\frac{1}{N}\sum_j e^{-\mathbf{R}_j\cdot\mathbf{k}}d_j, \tag{3}$$

$Z={\rm Tr}\langle e^{-\beta H}\rangle$ the partition function, and $i\nu_l=2i\pi lT$ the bosonic Matsubara frequency (the τ dependence of the operators is with respect to the full Hamiltonian). The Raman response is characterized in terms of the different spatial symmetries of the scattering amplitude. One can expand this function in a Fourier series, examine the contributions of the lowest components of the series, and compare them to experiment. Alternatively, one can start from a metallic Hamiltonian, and expand the Raman response in powers of the electronic vector potential. Under the assumption that the photon wavelength is much larger than the lattice spacing, this latter approach yields the following results for the Raman scattering amplitudes in two dimensions:

$$\gamma_{A_{1g}}(\mathbf{k})\approx\frac{\partial^2\epsilon(\mathbf{k})}{\partial k_x^2}+\frac{\partial^2\epsilon(\mathbf{k})}{\partial k_y^2}\approx-\epsilon(\mathbf{k}),$$

$$\gamma_{B_{1g}}(\mathbf{k})\approx\frac{\partial^2\epsilon(\mathbf{k})}{\partial k_x^2}-\frac{\partial^2\epsilon(\mathbf{k})}{\partial k_y^2}\approx\cos k_x-\cos k_y,$$

$$\gamma_{B_{2g}}(\mathbf{k})\approx\frac{\partial^2\epsilon(\mathbf{k})}{\partial k_x\partial k_y}\approx\sin k_x\sin k_y, \tag{4}$$

with $\epsilon(\mathbf{k})\propto\cos k_x+\cos k_y$ the electronic band structure. Note that the B_{2g} response vanishes for pure nearest-neighbor hopping, which is what we consider here (the band structure is just a sum of cosines; hence all mixed derivatives vanish). *The nonresonant B_{2g} Raman response then vanishes, because the lowest-order Raman scattering amplitude vanishes.*

The above forms can be generalized to the infinite-d limit for nonresonant scattering by noting that $\gamma(\mathbf{k})$ satisfies[13]

$$\gamma(\mathbf{k}) = \sum_{\alpha\beta} e_{i\alpha} \frac{\partial^2 \epsilon(\mathbf{k})}{\partial k_\alpha \partial k_\beta} e_{o\beta}, \tag{5}$$

with $\mathbf{e}_i(\mathbf{e}_o)$ the incoming (outgoing) photon polarization. In systems with hopping beyond nearest neighbors, it is not possible to project completely onto the A_{1g} sector with just one choice of polarizations, since either B_{1g} or B_{2g} sectors will always be mixed in; it is possible to project onto B_{1g} or B_{2g} with one measurement. In the infinite-dimensional limit, with nearest-neighbor hopping only, we can choose $\mathbf{e}_{i\alpha} = \mathbf{e}_{o\alpha} = 1$ for A_{1g}, $\mathbf{e}_{i\alpha} = 1$ and $\mathbf{e}_{o\alpha} = (-1)^\alpha$ for B_{1g}, and $\mathbf{e}_{i\alpha=\text{even}} = 0$, $\mathbf{e}_{i\alpha=\text{odd}} = 1$, $\mathbf{e}_{o\alpha=\text{even}} = 1$, and $\mathbf{e}_{o\alpha=\text{odd}} = 0$ for B_{2g}. The resulting Raman scattering amplitudes are

$$\gamma_{A_{1g}}(\mathbf{k}) \approx c - \epsilon(\mathbf{k}), \quad \gamma_{B_{1g}}(\mathbf{k}) \approx \frac{1}{\sqrt{d}} \sum_{i=1}^{d} (-1)^i \cos k_i, \tag{6}$$

and $\gamma_{B_{2g}}(\mathbf{k}) = 0$. Note that we include a constant term c in the A_{1g} amplitude, since it is allowed by symmetry.

The nonresonant Raman response in the B_{1g} channel has no vertex corrections[14,9] and is equal to the bare bubble. The key element needed to show this is that the irreducible charge vertex Γ is independent of momentum (since it is local). Hence, we must evaluate a summation over $\mathbf{k}$ of the form

$$\sum_{\mathbf{k}} \frac{1}{\sqrt{d}} \sum_{i=1}^{d} (-1)^i \cos k_i \frac{1}{X + \frac{2}{\sqrt{d}} \sum_{j=1}^{d} \cos k_j}, \tag{7}$$

which arises when solving the Dyson equation for the B_{1g} response (and we can assume without loss of generality that the imaginary part of X is greater than zero). Writing the fraction in Eq. (7) as the integral of an exponential,[15]

$$\frac{1}{X + \frac{2}{\sqrt{d}} \sum_{j=1}^{d} \cos k_j} = -i \int_0^\infty dz \exp\left[iz \left(X + \frac{2}{\sqrt{d}} \sum_{j=1}^{d} \cos k_j \right) \right], \tag{8}$$

allows us to decouple the summation over momentum to the sum over d identical terms, each multiplied by $(-1)^i$. This then vanishes for all even d and for odd d in the limit $d \to \infty$ (due to the $1/\sqrt{d}$ term). So the nonresonant B_{1g} response reduces to the evaluation of the bare bubble.

In the A_{1g} channel, the Raman scattering amplitude has the same symmetry as the irreducible charge vertex, so the corresponding summation over momentum does not vanish, and the nonresonant A_{1g} Raman response is renormalized by the irreducible charge vertex.

The Falicov-Kimball model can be solved exactly in the infinite-dimensional limit by using dynamical mean-field theory (see Ref. 16 for details). We summarize the main points to establish our notation. The local Green's function at the fermionic Matsubara frequency $i\omega_n = i\pi T(2n+1)$ is defined by

$$G_n = G(i\omega_n) = -\operatorname{Tr} T_\tau \int_0^\beta d\tau e^{i\omega_n \tau} \frac{\langle e^{-\beta H_{at}} d(\tau) d^\dagger(0) S(\lambda) \rangle}{Z}, \tag{9}$$

with

$$Z = Z_0(\mu) + e^{-\beta(E_f - \mu)} Z_0(\mu - U), \tag{10}$$

the atomic partition function expressed in terms of

$$Z_0(\mu) = \operatorname{Tr}_d \langle e^{-\beta H_0} S(\lambda) \rangle, \quad H_0 = -\mu d^\dagger d. \tag{11}$$

In the above equations, the atomic Hamiltonian H_{at} is the Hamiltonian of Eq. (1) restricted to one site, with $t^* = 0$, and all time dependence is with respect to H_{at}. The evolution operator $S(\lambda)$ satisfies

$$S(\lambda) = \exp\left[-\int_0^\beta d\tau \int_0^\beta d\tau' d^\dagger(\tau) \lambda(\tau - \tau') d(\tau') \right], \tag{12}$$

with $\lambda(\tau - \tau')$ a time-dependent atomic field adjusted to make the atomic Green's function equal to the local lattice Green's function. We define an effective medium by

$$G_0^{-1}(i\omega_n) = G_n^{-1} + \Sigma_n = i\omega_n + \mu - \lambda_n, \tag{13}$$

with Σ_n the local self-energy and λ_n the Fourier transformation of $\lambda(\tau)$. The trace in Eq. (9) can be evaluated directly to yield

$$G_n = w_0 G_0(i\omega_n) + w_1 [G_0^{-1}(i\omega_n) - U]^{-1}, \tag{14}$$

with $w_0 = 1 - w_1$,

$$w_1 = \exp[-\beta(E_f - \mu)] Z_0(\mu - U)/Z, \tag{15}$$

and

$$Z_0(\mu) = 2 e^{\beta\mu/2} \prod_{n=-\infty}^{\infty} \frac{i\omega_n + \mu - \lambda_n}{i\omega_n}. \tag{16}$$

The self-consistency relation needed to determine λ_n and G_n is to equate the local lattice Green's function to the atomic Green's function via

$$G_n = \int_{-\infty}^{\infty} d\epsilon \frac{\rho(\epsilon)}{i\omega_n + \mu - \Sigma_n - \epsilon}, \tag{17}$$

with $\rho(\epsilon) = \exp(-\epsilon^2)/\sqrt{\pi}$ the noninteracting density of states for the infinite-dimensional hypercubic lattice.

The iterative algorithm to solve for G_n starts with $\Sigma_n = 0$. Then Eq. (17) is used to find G_n, Eq. (13) is employed to extract the effective medium, Eq. (14) is used to find a new local Green's function, and then Eq. (13) is used to find the new self-energy. This sequence of steps is then repeated until it converges, which usually requires only about a dozen or so iterations. This algorithm can also be used on the real axis (with suitably modified equations) to directly solve for the Green's function and self-energy on the real axis.

Once the Green's functions are known, then the nonresonant Raman response can be calculated directly. The B_{1g} channel is simple, since we need only evaluate the bare bubble. Noting that the average of the square of the B_{1g} Raman scattering amplitude is 1/2 then yields

$$\chi_{B_{1g}}(i\nu_l) = -\frac{T}{2}\sum_n \frac{G(i\omega_n) - G(i\omega_{n+l})}{i\nu_l + \Sigma(i\omega_n) - \Sigma(i\omega_{n+l})} \tag{18}$$

for the Raman response on the imaginary axis. This formula can be easily analytically continued to the real axis by following the same procedure outlined in the calculation of the dynamical charge susceptibility:[17] rewrite the sum over Matsubara frequencies by a contour integral of advanced or retarded Green's functions and self-energies multiplied by the Fermi factor, and then deform the contours to the real axis picking up any poles in the complex plane. Under the assumption that there are no extra poles when the contours are deformed, one ends up with the following expression for the B_{1g} response:

$$\chi_{B_{1g}}(\nu) = \frac{-i}{4\pi}\int_{-\infty}^{\infty} d\omega \Bigg\{ f(\omega)\frac{G(\omega) - G(\omega+\nu)}{\nu + \Sigma(\omega) - \Sigma(\omega+\nu)} - f(\omega+\nu)\frac{G^*(\omega) - G^*(\omega+\nu)}{\nu + \Sigma^*(\omega) - \Sigma^*(\omega+\nu)} - [f(\omega) - f(\omega+\nu)]\frac{G^*(\omega) - G(\omega+\nu)}{\nu + \Sigma^*(\omega) - \Sigma(\omega+\nu)} \Bigg\}, \tag{19}$$

with $f(\omega) = 1/[1+\exp(\beta\omega)]$ the Fermi function. We verify that this expression is indeed accurate, by using the spectral formula to calculate the Raman response on the imaginary axis and comparing it to the result directly calculated from the expression in Eq. (18). We find that the results rarely differ by more than 1 part in 1000, confirming the accuracy of the analytic continuation (we believe, but cannot prove, that no additional poles exist in the complex plane, which would mean the analytic continuation is exact).

We can use the expression in Eq. (19) to prove the Shastry-Shraiman relation. Using the identity that relates the local Green's function on the lattice to the self-energy in Eq. (17) (but evaluated on the real axis rather than the imaginary axis) yields

$$\frac{G(\omega) - G(\omega+\nu)}{\nu + \Sigma(\omega) - \Sigma(\omega+\nu)} = \int_{-\infty}^{\infty} d\epsilon \frac{\rho(\epsilon)}{[\omega + \mu - \Sigma(\omega) - \epsilon][\omega + \nu + \mu - \Sigma(\omega+\nu) - \epsilon]}. \tag{20}$$

Employing this identity and related ones for the advanced Green's functions in Eq. (19) produces

$$\chi_{B_{1g}}(\nu) = \frac{1}{2\pi}\int_{-\infty}^{\infty} d\omega \int_{-\infty}^{\infty} d\epsilon \rho(\epsilon) \times \Bigg\{ \frac{f(\omega)}{\omega + \nu + \mu - \Sigma(\omega+\nu) - \epsilon}\,\mathrm{Im}\frac{1}{\omega + \mu - \Sigma(\omega) - \epsilon} + \frac{f(\omega+\nu)}{\omega + \mu - \Sigma^*(\omega) - \epsilon}\,\mathrm{Im}\frac{1}{\omega + \nu + \mu - \Sigma(\omega+\nu) - \epsilon} \Bigg\}. \tag{21}$$

Using the definition of the spectral function

$$A(\epsilon, \omega) = -\frac{1}{\pi}\,\mathrm{Im}\frac{1}{\omega + \mu - \Sigma(\omega) - \epsilon} \tag{22}$$

and taking the imaginary part of Eq. (21) then yields

$$\mathrm{Im}\,\chi_{B_{1g}}(\nu) = \frac{\pi}{2}\int_{-\infty}^{\infty} d\omega \int_{-\infty}^{\infty} d\epsilon \rho(\epsilon) \times [f(\omega) - f(\omega+\nu)] A(\epsilon, \omega) A(\epsilon, \omega+\nu), \propto \nu\sigma(\nu), \tag{23}$$

which is the Shastry-Shraiman relation—the imaginary part of the nonresonant B_{1g} Raman response is proportional to the frequency ν times the optical conductivity $\sigma(\nu)$. This conclusion comes from comparing the integration in Eq. (23) to the well-known result for the optical conductivity on the infinite-d hypercubic lattice.[18] Note that this final formula for the Raman response depends only on the shape of the spectral function. Since the derivation was model independent (like the derivation of the optical conductivity[18]), this form for the nonresonant B_{1g} Raman response holds for all models. (Similarly, in models with next-nearest-neighbor hopping, one can also show that the nonresonant B_{2g} response also satisfies the Shastry-Shraiman relation.) We note that this is a consequence of the momentum-independent self-energy—any dependence of the self-energy on momentum will generally violate the Shastry-Shraiman relation, although it may still be an accurate approximation.

The A_{1g} response is more complicated, because it requires a proper treatment of the vertex contributions. Fortunately, the charge vertex for the Falicov-Kimball model is well known[17] and assumes a simple form (for $i\nu_l \neq 0$)

$$\Gamma(i\omega_m, i\omega_n; i\nu_l) = \delta_{m,n}\frac{1}{T}\frac{\Sigma(i\omega_n) - \Sigma(i\omega_{n+l})}{G(i\omega_n) - G(i\omega_{n+l})}. \tag{24}$$

Hence, the Raman response in the A_{1g} channel can be found by solving the relevant Dyson's equation, using the above form of the charge vertex. The set of Feynman diagrams is shown in Figs. 1 and 2. Note that we have to solve these two coupled equations for the A_{1g} Raman response.

The difference between the two diagrams shown in Figs. 1 and 2 is the number of factors of the Raman scattering amplitude γ; the nonresonant Raman response requires the dressed response that has only one power of γ—this dressed response satisfies a simple Dyson equation, shown in Fig. 2.

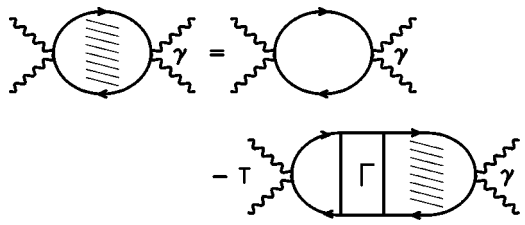

FIG. 2. Supplemental Feynman diagrams for the nonresonant A_{1g} Raman response. These diagrams are identical to those in Fig. 1 except they have one fewer power of γ.

We denote the dressed response function in Fig. 2 by $\chi'(i\omega_m, i\omega_n; i\nu_l)$. Then a straightforward evaluation of the Feynman diagrams and a solution of the Dyson equation produces

$$\chi'(i\omega_m, i\omega_n; i\nu_l) = \frac{\delta_{mn}\chi_0'(i\omega_m; i\nu_l)}{1+\chi_0(i\omega_m; i\nu_l)T\Gamma(i\omega_m, i\omega_m; i\nu_l)}, \tag{25}$$

with the irreducible charge vertex function found in Eq. (24),

$$\chi_0(i\omega_n; i\nu_l) = -\frac{G(i\omega_n) - G(i\omega_{n+l})}{i\nu_l + \Sigma(i\omega_n) - \Sigma(i\omega_{n+l})} \tag{26}$$

and

$$\chi_0'(i\omega_n; i\nu_l) = -\frac{c(G_n - G_{n+l}) - Z_n G_n + Z_{n+l} G_{n+l}}{i\nu_l + \Sigma_n - \Sigma_{n+l}}. \tag{27}$$

Here we used the notation $Z_n = i\omega_n + \mu - \Sigma(i\omega_n)$. Now, knowledge of χ' allows us to solve for the Raman response in Fig. 1. The end result is

$$\chi_{A_{1g}}(i\nu_l) = T\sum_n \frac{\overline{\chi_0}(i\omega_n; i\nu_l) - [\chi_0(i\omega_n; i\nu_l) + G_n G_{n+l}]T\Gamma(i\omega_n, i\omega_n; i\nu_l)}{1+\chi_0(i\omega_n; i\nu_l)T\Gamma(i\omega_n, i\omega_n; i\nu_l)}, \tag{28}$$

where the charge vertex is found in Eq. (24), the bare susceptibility χ_0 is found in Eq. (26), and the other bare susceptibility $\overline{\chi_0}$ (which is where all of the c dependence lies) is

$$\begin{aligned}\overline{\chi_0}(i\omega_n; i\nu_l) = [&-c^2(G_n - G_{n+l}) + 2c(Z_n G_n - Z_{n+l} G_{n+l}) \\ &+ Z_n - Z_{n+l} - Z_n^2 G_n + Z_{n+l}^2 G_{n+l}]/[i\nu_l + \Sigma_n \\ &- \Sigma_{n+l}].\end{aligned} \tag{29}$$

Surprisingly, all of the c dependence actually drops out of the nonresonant A_{1g} Raman response (as it does in conventional metals[7]). This can be seen by substituting the representations for χ_0 and Γ into the denominator in the first term of Eq. (28). One finds that the summation for the first term can then be written in the general form $\Sigma_n(Y_n - Y_{n+l})/i\nu_l$, which vanishes since the individual summations converge and one can change the summation index $n \to n+l$ in the first term [we similarly note that $\Sigma_n(\Sigma_n - \Sigma_{n+l}) = 0$]. Hence we arrive at the final form for the nonresonant A_{1g} Raman response:

$$\begin{aligned}\chi_{A_{1g}}(i\nu_l) &= \frac{T}{i\nu_l}\sum_n \frac{(\Sigma_n - \Sigma_{n+l})G_n G_{n+l}}{\chi_0(i\omega_n; i\nu_l)} \\ &= \frac{T}{i\nu_l}\sum_n \frac{(\Sigma_n - \Sigma_{n+l})(i\nu_l + \Sigma_n - \Sigma_{n+l})}{G_{n+l}^{-1} - G_n^{-1}}.\end{aligned} \tag{30}$$

It is a straightforward exercise to perform a similar analytic continuation of this expression. The result is

$$\begin{aligned}\chi_{A_{1g}}(\nu) = \frac{i}{2\pi\nu}\int_{-\infty}^{\infty} d\omega \Bigg\{ & f(\omega)\frac{[\Sigma(\omega) - \Sigma(\omega+\nu)][\nu + \Sigma(\omega) - \Sigma(\omega+\nu)]}{G^{-1}(\omega+\nu) - G^{-1}(\omega)} \\ & - f(\omega+\nu)\frac{[\Sigma^*(\omega) - \Sigma^*(\omega+\nu)][\nu + \Sigma^*(\omega) - \Sigma^*(\omega+\nu)]}{G^{-1*}(\omega+\nu) - G^{-1*}(\omega)} \\ & - [f(\omega) - f(\omega+\nu)]\frac{[\Sigma^*(\omega) - \Sigma(\omega+\nu)][\nu + \Sigma^*(\omega) - \Sigma(\omega+\nu)]}{G^{-1}(\omega+\nu) - G^{-1*}(\omega)}\Bigg\}.\end{aligned} \tag{31}$$

B. Resonant Raman response

Resonant Raman scattering arises from a fourth-order process with respect to the photon vector potential. One way to view this scattering is to "separate" the two-photon-two-electron vertex of nonresonant Raman scattering in Fig. 1 into two single-photon-two-electron vertices. Keeping in

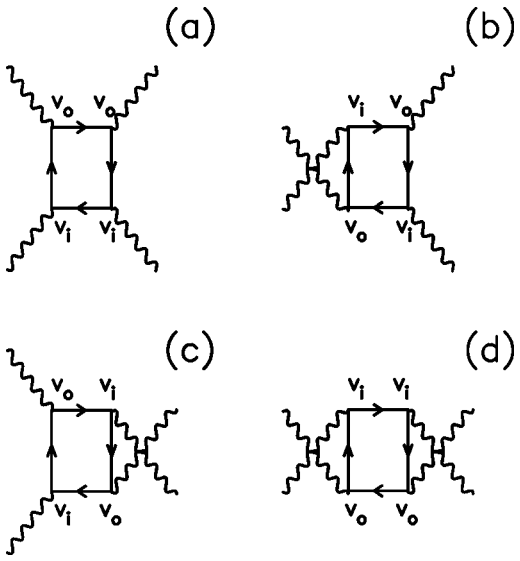

FIG. 3. Bare resonant Raman scattering diagrams. The (a) uncrossed, (b) first partially crossed, (c) second partially crossed, and (d) fully crossed diagrams are all shown. The straight lines are momentum-dependent Green's functions, the wiggly lines are photon propagators, and the vertex factors are the dot product of the photon polarization with the Fermi velocity as described in the text ($v_i = \mathbf{e}_i \cdot \mathbf{v}$, $v_o = \mathbf{e}_o \cdot \mathbf{v}$). Note that the two partially crossed diagrams (b) and (c) are equal to each other.

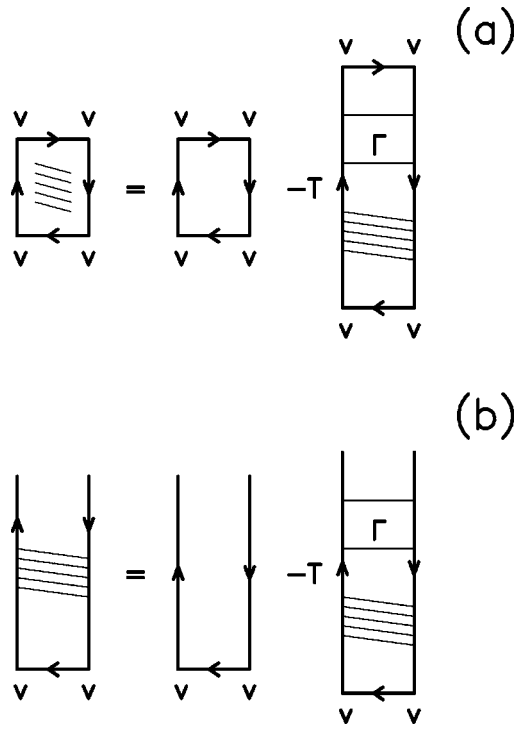

FIG. 4. Renormalized resonant Raman scattering diagrams for Figs. 3(a) and 3(d) in the B_{1g} and B_{2g} channels. We suppress the photon lines that are explicitly shown in Fig. 3, for simplicity. In (a) one has the diagrams for the Raman response, while in (b) the supplemental Dyson equation needed to solve for the dressed Raman response is given. The only difference for the B_{1g} and B_{2g} channels is the choice of polarization vectors $\mathbf{e}_i$ and $\mathbf{e}_o$, and we have suppressed the incoming and outgoing indices on the vertices v. The symbol Γ denotes the local irreducible charge vertex. Note that only the direct and exchange diagrams [Figs. 3(a) and 3(d)] are renormalized.

mind the direct and exchange possibilities results in four distinct bare resonant Raman scattering diagrams, which are depicted in Fig. 3: (a) the uncrossed (direct) diagram, (b) the first partially crossed diagram, (c) the second partially crossed diagram, and (d) the fully crossed (exchange) diagram. In all relevant cases, the partially crossed diagrams (b) and (c) are equal to each other.

In general, the Raman vertices for resonant scattering involve expectation values of the momentum operator between the conduction band and the excited states. However, in the single-band model, the Raman vertices in Fig. 3 are equal to the dot product of the photon polarization vector $\mathbf{e}$ with Fermi velocity $\mathbf{v}$:

$$v_\alpha = \frac{\partial \epsilon(\mathbf{k})}{\partial k_\alpha} = \frac{t^*}{\sqrt{d}} \sin k_\alpha . \tag{32}$$

Again, we distinguish between the incoming photon polarization $\mathbf{e}_i$ and the outgoing photon polarization $\mathbf{e}_o$. The different symmetry channels are projected by appropriate choice of the polarization vectors. We choose $\mathbf{e}_{i\alpha} = \mathbf{e}_{o\alpha} = 1$ for A_{1g}, $\mathbf{e}_{i\alpha} = 1$, and $\mathbf{e}_{o\alpha} = (-1)^\alpha$ for B_{1g}, and $\mathbf{e}_{i\alpha=\text{even}} = 0$, $\mathbf{e}_{i\alpha=\text{odd}} = 1$, $\mathbf{e}_{o\alpha=\text{even}} = 1$, and $\mathbf{e}_{o\alpha=\text{odd}} = 0$ for B_{2g}. It is important to note that in all cases a single factor of $\mathbf{e} \cdot \mathbf{v}$ is an odd function of $\mathbf{k}$, so the only way to get nonzero summations over momentum is to have an even number of $\mathbf{e} \cdot \mathbf{v}$ factors in any given integration.

In general, the bare resonant Raman scattering diagrams must be renormalized by attaching appropriate irreducible charge vertex functions (and higher-order generalizations, if possible) to all relevant Green's function legs. Since all $\mathbf{e} \cdot \mathbf{v}$ factors are odd in $\mathbf{k}$ and the irreducible charge vertex has A_{1g} symmetry, there can be no renormalization of any single vertex. Similarly, one can argue that there are no three-particle or four-particle vertex renormalizations possible either. The only possibility is a two-particle vertex that connects opposite Green's function lines. In the A_{1g} resonant Raman scattering channel, all possible vertical and horizontal renormalizations of each bare diagram are possible. For the B_{1g} and B_{2g} channels, there are simplifications. One can quickly verify that in both of those cases the product $\mathbf{e}_i \cdot \mathbf{v} \mathbf{e}_o \cdot \mathbf{v}$ is orthogonal to the A_{1g} symmetry, so the partially crossed diagrams (b) and (c) cannot have any renormalization either. Furthermore, this also implies that attaching a vertical charge vertex to either the (a) or the (d) diagram vanishes for the same reason. But a horizontal attachment of the vertex is possible in both the (a) and (d) diagrams. Hence, the renormalized resonant Raman scattering in both the B_{1g} and B_{2g} channels is described by the coupled set of equations in Fig. 4. A similar, but more complicated, set of diagrams is needed for the A_{1g} channel, where renormalizations are present on both the vertical and horizontal pairs of legs for all diagrams. We do not show those Feynman diagrams here.

Evaluation of these diagrams and their analytic continuation to the real axis is tedious. We leave that task for a future

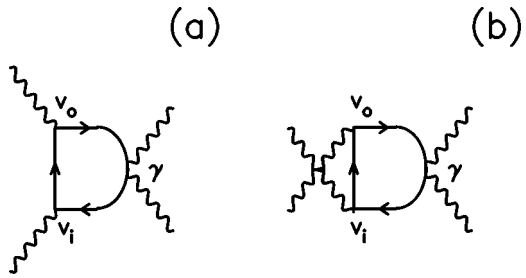

FIG. 5. Bare mixed Raman response. The single-photon vertices are multiplied by the respective factor of the polarization vector dotted into the Fermi velocity, while the two-photon vertex is multiplied by the corresponding Raman scattering amplitude. Note that no renormalization is possible for the B_{1g} channel, but the diagram is renormalized in the A_{1g} channel.

publication. But we do note that both of the renormalized diagrams (a) and (d) of Fig. 3 will have the zero-frequency ($i\nu_l=0$) piece of the irreducible charge vertex renormalizing them. This is the nondiagonal piece of the charge vertex, and it can get large when the system is tuned to lie near a phase-separation transition. Hence, we expect the resonant Raman scattering to be enhanced whenever one is close to a phase separation. Note that this enhancement will occur for all photon frequencies, since the zero-frequency vertex couples all such diagrams; this implies that one will not see this effect by tuning through a resonant frequency.

C. Mixed Raman response

The mixed Raman response comes from the cross terms between the linear and quadratic terms in the vector potential. As such, these diagrams have two single-photon–two-electron vertices and one two-photon–two-electron vertex. Since the B_{2g} Raman scattering amplitude vanishes for nearest-neighbor hopping on a hypercubic lattice, there is no mixed Raman response for that channel. The bare mixed Raman response is shown in Fig. 5. There are two possible diagrams corresponding to the direct or exchange processes. In the B_{1g} channel, the dressed mixed response is equal to the bare mixed response, since the irreducible charge vertex cannot be inserted anywhere. For the A_{1g} channel, the bare mixed response is renormalized by the irreducible charge vertex in a similar way to how it renormalized the nonresonant Raman response. We do not present any numerical results for the mixed Raman response here, but will do so in another publication. It turns out that one can show that in the B_{1g} channel with nearest-neighbor hopping only, the mixed response is a $1/d$ correction and can be neglected; it cannot be neglected for the A_{1g} sector. The $1/d$ correction for B_{1g} arises from the fact that the summation over momentum has a ''form factor'' proportional to $\cos(k_i)(-1)^i \sin^2(k_j)(-1)^j$. This term cancels when summed over i and j except for $i=j$. This latter constraint forces the mixed diagram to be a $1/d$ correction. In the A_{1g} case, there are no factors of (-1), so the terms with all i and j contribute, and it is an $O(1)$ term.

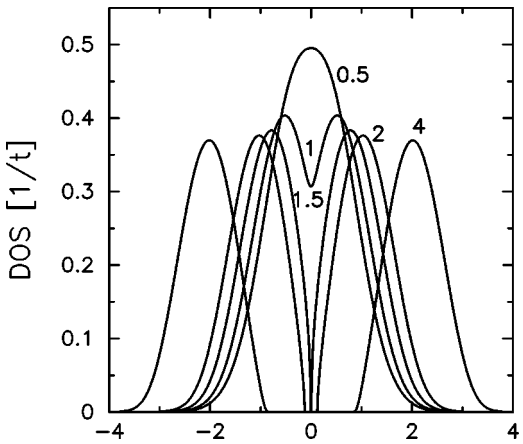

FIG. 6. Interacting density of states for the Falicov-Kimball model. Results are shown for $U=0.5$, 1, 1.5, 2, and 4 (the numbers in the figure label the value of U). Note how the system first develops a pseudogap (1.0) before the metal-insulator transition at $U=1.5$. The density of states is independent of temperature.

III. RESULTS

The Falicov-Kimball model has a ground state that is not a Fermi liquid because the lifetime of a quasiparticle is finite at the Fermi energy. In addition, the imaginary part of the self-energy has the wrong sign of curvature to be a Fermi liquid. We study the model at half filling. As U increases, the system first enters a pseudogap phase, where spectral weight is depleted near the chemical potential, and then undergoes a metal-insulator transition (the pseudogap phase is possible because the ground state is not a Fermi liquid). The interacting density of states (DOS) is, however, temperature independent for fixed U and fixed electron fillings.[19] It is plotted in Fig. 6 for a range of values of U: $U<0.65$ corresponds to a weakly correlated metal, while a pseudogap phase appears for $0.65<U<1.5$ moving through a quantum-critical point at $U=1.5$ to the insulator phase $U>1.5$ (we neglect all possible charge-density-wave phases here).

In Fig. 7(a) we plot the nonresonant B_{1g} Raman response at a fixed temperature $T=0.5$ for different values of U. For small values of U, a small scattering intensity is observed due to the weak interaction among ''quasiparticles,'' providing a small region of phase space allowable for pair scattering. The peak of the response reflects the dominant energy scale for scattering, as is well known in metals,[7] and the high-energy tail is the cutoff determined by the finite-energy band. This shape is also understandable from the Shastry-Shraiman relation—since the optical conductivity is a Lorentzian, the Raman response is just proportional to $a\nu/[\nu^2+a^2]$, which assumes the above form. As U increases, the low-frequency response is depleted as spectral weight gets shifted into a large charge-transfer peak at a frequency $\sim U$. The charge-transfer peak begins to appear for values of U for which the DOS is still finite at the Fermi level ($U=1$) and becomes large in this pseudogap phase before growing even larger in the insulating phase. Notice how low-frequency spectral weight remains even as one is well on the insulating side of the quantum-critical point ($U=4$) and at a temperature T much lower than the gap. It is

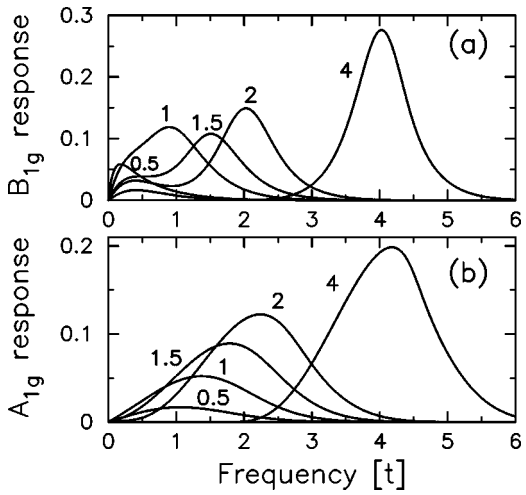

FIG. 7. Nonresonant (a) B_{1g} and (b) A_{1g} Raman response for different values of U at $T=0.5$. The Raman response is measured in arbitrary units. Notice how the vertex corrections suppress the low-frequency spectral weight in the A_{1g} channel.

these spectral features that are characteristically seen in the experiments and which can only be seen in a theory that approaches the quantum-critical point.

In Fig. 7(b), we show the nonresonant A_{1g} Raman response. As shown above, the A_{1g} response is independent of the value of c. The general behavior is similar to that of the B_{1g} channel except (i) at weak coupling the Raman scattering is more symmetric and pushed to higher energy, (ii) the vertex corrections suppress all nontrivial low-frequency Raman response, and (iii) the widths of the charge-transfer peaks are enhanced.

Since the Raman response displays anomalous features on the insulating side of the metal-insulator transition, we first present results for $U=2$, just on the insulating side of the quantum critical point. In Fig. 8(a), we plot the temperature dependence. The total spectral weight increases dramatically with decreasing temperature as charge-transfer processes become more sharply defined. At the same time, the low-frequency response depletes with lowering temperatures, vanishing at a temperature which is on the order of the $T=0$ insulating gap (we are unable to analytically estimate the crossover temperature). This behavior is precisely what is seen in experiments on[3] FeSi and on[4] underdoped $La_{2-x}Sr_xCuO_4$ at low temperatures where both the isosbestic point and the low-temperature spectral weight depletion can be seen. Similar results are also seen[2] in SmB_6, but a low-energy peak also develops in that material at low temperatures. In the A_{1g} channel [Fig. 8(b)], we see the same sharpening of the charge-transfer peak at low T, but the low-energy response is much smaller and changes much more slowly with T (but, in fact, increases as T is lowered).

If one were to interpret the temperature at which the B_{1g} Raman spectral weight starts to deplete as the ''transition temperature'' T_c and the range of frequency over which the weight is depleted as the gap Δ, then one would conclude that near the quantum-critical point $2\Delta/k_BT_c \gg 1$. This is because the ''T_c'' is effectively determined by the gap in the single-particle density of states (which is small near the quantum critical point), while the ''Δ'' is determined by the width of the lower Hubbard band (which remains finite at the quantum-critical point); hence the ratio can become very large near the quantum-critical point (and should decrease in the large-U limit).

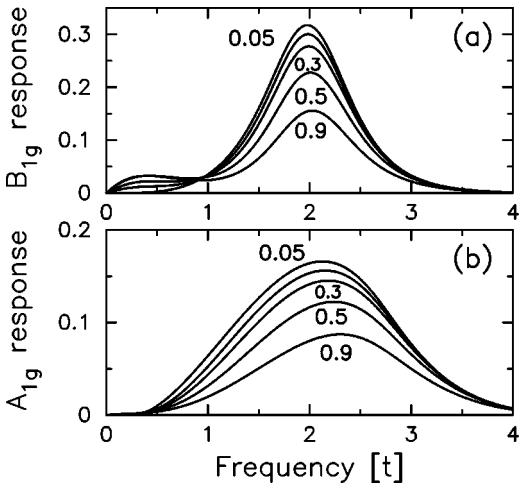

FIG. 8. (a) Nonresonant B_{1g} Raman response for a range of temperatures ($T=0.05,0.2,0.3,0.5,0.9$) for $U=2$ (which lies just on the insulating side of the metal-insulator transition) and (b) nonresonant A_{1g} Raman response for the same temperatures at $U=2$. The lines are labeled by their temperature (except for $T=0.2$ which is unlabeled). Note how the B_{1g} response has low-frequency spectral weight that develops rapidly at an onset temperature of $T\approx 0.2$ (the low-frequency responses at $T=0.5$ and $T=0.9$ overlap) and note the isosbestic point at $\nu\approx 1$. The ratio of the range in frequency over which the low-frequency weight increases and the onset temperature is about 5. There are no anomalous features in the A_{1g} spectrum.

The nonresonant Raman response is plotted in Fig. 9 for a number of different temperatures at $U=1$. Note how the B_{1g} response has nontrivial low-energy spectral weight, even though it is not completely separated from the charge-transfer processes. Even in this case, one can see the low-temperature development of an isosbestic point near $U/2$ for temperatures below about $T=0.3$. As the low-energy spectral weight is depleted, the peak becomes more symmetric in shape. In the A_{1g} channel, the response sharpens, and the peak moves to lower energy as the temperature is lowered. In fact, the low-energy spectral weight actually increases as T is lowered. There is no indication of a separation of the response into low- and high-energy features that have a different temperature dependence (as seen for the B_{1g} response).

The B_{1g} spectral-weight transfer from low frequencies to the charge-transfer peak as a function of temperature can be quantified by separating the Raman response into two regions determined by the isosbestic point and plotting the ratio of the low-frequency spectral weight at temperature T to the low-frequency spectral weight at $T=0.95$ versus reduced temperature $T/0.95$ (Fig. 10). Choosing $U/2$ as the location of the isosbestic point (which divides the low-frequency and high-frequency regions), we find that the reduction of spectral weight from high to low temperatures is over 50% even in the weak pseudogap phase, and decreases by well over three orders of magnitude as U increases into the insulating phase ($U=4$).

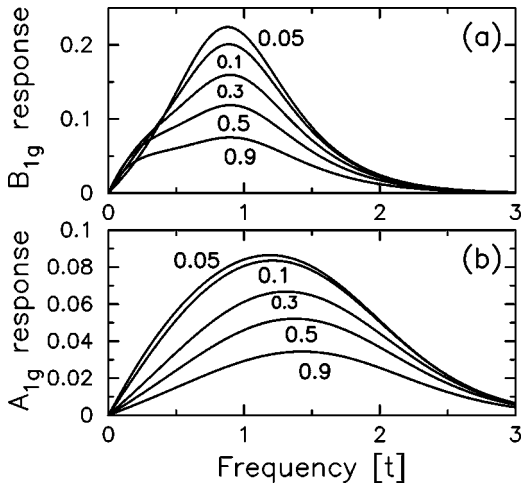

FIG. 9. Nonresonant (a) B_{1g} and (b) A_{1g} Raman response at $U=1$ for $T=0.9$, 0.5, 0.3, 0.1, 0.05. The lines are labeled by the temperature. Note how the B_{1g} response develops an isosbestic point at low temperatures, but the low-frequency depletion is more modest here than in the insulating phase. The A_{1g} response has no anomalous features, but the peak of the response moves to lower energies as the Raman response sharpens at low temperature. In the moderate to low-frequency range, the Raman response increases as T is lowered.

The origin of the isosbestic point in the nonresonant B_{1g} response is mysterious, but can be motivated by the Shastry-Shraiman relation.[1] Since the optical conductivity satisfies a sum rule, the appearance of an isosbestic point there is not surprising, as any decrease in low-frequency spectral weight must be compensated by a corresponding increase in high-frequency spectral weight, so one might expect there to be a frequency where the response does not depend on T (of course this does not establish that an isosbestic point must exist; it just motivates such an existence). The isosbestic point in the B_{1g} Raman response then follows from the Shastry-Shraiman relation, since multiplying the optical conductivity by a frequency will not modify the appearance of an isosbestic point.

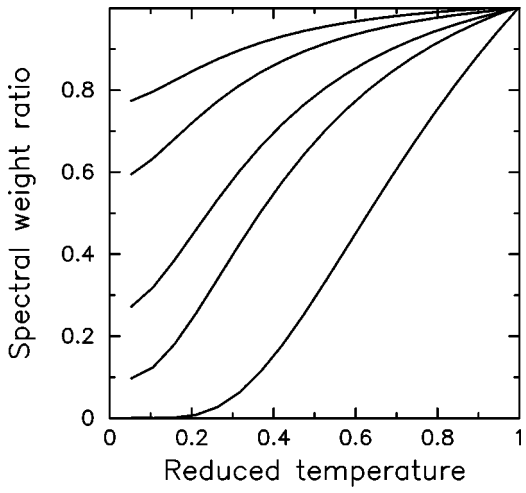

FIG. 10. Ratio of low-frequency spectral weight at temperature T to the low-frequency spectral weight at $T=0.95$ plotted vs reduced temperature $T/0.95$ for different values of U. The values of U are 0.5, 1, 1.5, 2, and 4, and the curves correspond to increasing values of U starting at the top with 0.5 and running to the bottom at 4. Note how the sharpening of the Raman response as T is lowered results in significant reductions to the low-frequency spectral weight even in the metallic case. In the strong insulator phase, the spectral weight decreases by over three orders of magnitude ($U=4$).

We attribute the presence of anomalous low-frequency and low-temperature response in a system which is a strongly correlated insulator to the appearance of thermally activated transport channels (indeed, the only temperature dependence to the Raman response comes from Fermi factors in an integral). In the insulating phase at zero temperature, the only available intermediate states created by the light must involve double-site occupancy of a conduction and a localized electron, with an energy cost of U. This gives the large charge-transfer peak. As the temperature is increased, double occupancy can occur and as a result light can scatter electrons to hop between adjacent unoccupied states either directly or via virtual double occupancies. The number of electrons which can scatter in this fashion increases with increasing temperature, leading to an increase in the low-frequency spectral weight. The frequency range for this low-frequency Raman response is determined by the lower Hubbard bandwidth, which is typically much larger than the temperature at which these features first appear.

There is also a more mathematical explanation to the low-frequency spectral response. If we examine the integral for the B_{1g} Raman response in Eq. (19), we note three important points: (i) the imaginary part of the Raman response is proportional to the real part of the integrand [the terms within the braces in Eq. (19)], (ii) the integrand vanishes if the Green's functions (and self-energy) at ω and $\omega+\nu$ are both real, and (iii) all temperature dependence arises from the Fermi factors, since both G and Σ are temperature independent. In the insulating regime, the DOS breaks into two pieces, a lower subband centered at $-U/2$ with a width of $O(1)$ and an upper subband at $U/2$ with a width of $O(1)$. The Green's functions are complex only when the frequency argument lies within one of the bands. Hence there are two main contributions to the Raman response: (i) intraband processes, where $\omega\approx -U/2$ or $U/2$ and $\nu\approx 1$, and (ii) interband processes, where $\omega\approx -U/2$ and $\nu\approx U$. The interband processes, with $\nu\approx U$, are what give rise to the charge-transfer peaks seen in the Raman response; these processes survive even at $T=0$. The intraband processes, with $\nu\approx 1$, give rise to the low-frequency spectral features. At low temperatures, these features are proportional to $f(\omega)-f(\omega+\nu)$ which can be approximated by $\exp(-U/2T)[1-\exp(\nu/T)]$ in the insulating phase. Hence, we expect the low-frequency spectral weight to be proportional to $\exp(-U/2T)$ in the large-U limit. In the A_{1g} channel, the charge vertex makes the integrand more complicated to analyze (but the response still separates into interband and intraband processes), and the vertex corrections end up ultimately suppressing the low-frequency response.

Last, we plot the inverse slope of the Raman response in Fig. 11 as a function of temperature for different values of U. The inverse Raman slope is the reciprocal of the slope of the Raman response in the limit as $\omega\rightarrow 0$. Since the self-energy is temperature independent, we might expect a constant Ra-

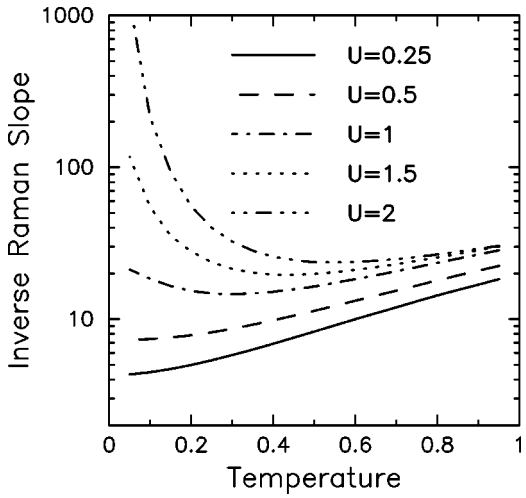

FIG. 11. Inverse Raman slope as a function of temperature. The inverse Raman slope measures the scattering rate of the ''quasiparticles'' of a correlated metal. As the system enters the pseudogap phase, the inverse slope starts to increase at low temperatures, increasing dramatically as one enters the correlated insulator ($U=2$).

man slope as a function of temperature, as is the case with a disordered Fermi liquid. However, this is not the case due to the formation of a thermally generated band for scattering. For small values of U, the temperature dependence of the Raman inverse slope is weak due to the temperature independence of the self-energy. However, as the single-particle bands begin to separate, the relevance of thermally generated double occupancies becomes more pronounced and the inverse slope rapidly rises at low temperatures. As the system becomes more insulating, the low-temperature inverse slope increases dramatically due to the depletion of the low-frequency spectral weight. As U increases from the pseudogap phase into the insulating phase, the temperature dependence of the Raman inverse slope indicates the formation of gapped excitations (assuming the form $T[1+\cosh(\Delta/\{2T\})]$, with Δ the gap in the single-particle DOS). Such behavior has been seen in the underdoped cuprate materials.

IV. CONCLUSIONS

The electronic Raman response of a wide variety of correlated materials (on the insulating side of the metal-insulator transition) displays similar anomalous features, which point to a common explanation. In our results, we have shown how to see these anomalies in the B_{1g} channel by solving the Falicov-Kimball model. We saw that the Raman response ultimately depended only on the single-particle density of states. In more complicated correlated models, the metallic single-particle density of states can have an additional Fermi liquid peak at low frequencies which will add new features to the Raman response,[20] but on the insulating side of the transition, where most of the anomalous behavior is seen, the single-particle density of states must be similar to that of the Falicov-Kimball model (except for some additional weak temperature dependence of the interacting DOS), since an insulator has no low-energy spectral weight. Hence, these anomalous Raman scattering results are expected to be essentially model independent (since they only depend on the interacting DOS).

In this work, we also illustrated how one can calculate both the resonant and the mixed Raman scattering responses as well. We showed how the bare diagrams are renormalized for the different symmetry sectors, but did not perform any numerical calculations here.

Our theoretical results compare quite favorably to the experimental results seen in a variety of different materials ranging from mixed-valence compounds[2] to Kondo insulators[3] to the underdoped high-temperature superconducting oxides.[4–6] The experimental data illustrate the three characteristic features seen in our theory: (i) there is a rapid rise in the low-frequency spectral weight at low temperatures (at the expense of the high-frequency spectral weight), (ii) there is an isosbestic point, and (iii) the range of frequency over which the low-frequency weight appears is much larger than the onset temperature, where it is first seen. Our model always produces an isotropic gap, so we are unable to illustrate the symmetry-selective behavior seen in the copper oxides where only the B_{1g} response is anomalous and the A_{1g} and B_{2g} responses are metallic. But our results do indicate a ''universality'' and model independence of the Raman response on the insulating side of, but in close proximity to, a quantum-critical point. We believe this is the reason why so many different materials show the same generic behavior in their electronic Raman scattering.

In future work we will examine nonresonant B_{1g} Raman scattering in the Hubbard model[20] and will examine resonant and mixed Raman scattering effects in the Falicov-Kimball model.

ACKNOWLEDGMENTS

J.K.F. acknowledges support of the National Science Foundation under Grant DMR-9973225. T.P.D. acknowledges support from the National Research and Engineering Council of Canada. We also acknowledge useful discussions with S.L. Cooper, R. Hackl, J.C. Irwin, M.V. Klein, P. Miller, A. Shvaika, and V. Zlatić. We also thank S.L. Cooper, R. Hackl, and J.C. Irwin for sharing their data with us. J.K.F. thanks the hospitality of the IBM, Almaden Research Center, where this work was completed.

[1] B. S. Shastry and B. I. Shraiman, Phys. Rev. Lett. **65**, 1068 (1990); Int. J. Mod. Phys. B **5**, 365 (1991).

[2] P. Nyhus, S. L. Cooper, Z. Fisk, and J. Sarrao, Phys. Rev. B **52**, R14 308 (1995); **55**, 12 488 (1997).

[3] P. Nyhus, S. L. Cooper, and Z. Fisk, Phys. Rev. B **51**, R15 626 (1995).

[4] X. K. Chen, J. G. Naeini, K. C. Hewitt, J. C. Irwin, R. Liang, and W. N. Hardy, Phys. Rev. B **56**, R513 (1997); J. G. Naeini, X. K.

Chen, J. C. Irwin, M. Okuya, T. Kimura, and K. Kishio, *ibid.* **59**, 9642 (1999).

[5] M. Opel, R. Nemetschek, C. Hoffmann, R. Philipp, P. F. Müller, R. Hackl, I. Tütto, A. Erb, B. Revaz, E. Walker, H. Berger, and L. Forró, Phys. Rev. B **61**, 9752 (2000).

[6] M. Rübhausen, O. A. Hammerstein, A. Bock, U. Merkt, C. T. Rieck, P. Guptasarma, D. G. Hinks, and M. V. Klein, Phys. Rev. Lett. **82**, 5349 (1999); S. Sugai, and T. Hosokawa, *ibid.* **95**, 1112 (2000).

[7] To our knowledge no comprehensive review of electronic Raman scattering in metals exists. General ideas are covered in P. M. Platzmann and N. Tzoar, Phys. Rev. **136**, A11 (1964); A. A. Abrikosov and V. M. Genkin, Zh. Éksp. Teor. Fiz. **40**, 842 (1973) [Sov. Phys. JETP **38**, 417 (1974)]; A. Zawadowski and M. Cardona, Phys. Rev. B **42**, 10 732 (1990); T. P. Devereaux and A. P. Kampf, *ibid.* **59**, 6411 (1999).

[8] A. V. Chubukov and D. M. Frenkel, Phys. Rev. B **52**, 9760 (1995).

[9] J. K. Freericks and T. P. Devereaux, J. Condens. Phys. (Ukraine) **4**, 149 (2001); and (unpublished).

[10] L. M. Falicov and J. C. Kimball, Phys. Rev. Lett. **22**, 997 (1969).

[11] M. S. Laad, L. Craco, and E. Müller-Hartmann, Phys. Rev. B (to be published); cond-mat/9911378 (unpublished).

[12] W. Metzner and D. Vollhardt, Phys. Rev. Lett. **62**, 324 (1989).

[13] A. A. Abrikosov and V. M. Genkin, Zh. Éksp. Teor. Fiz. **40**, 842 (1973) [Sov. Phys. JETP **38**, 417 (1974)].

[14] A. Khurana, Phys. Rev. Lett. **64**, 1990 (1990).

[15] E. Müller-Hartmann, Z. Phys. B **74**, 507 (1989); **76**, 211 (1989).

[16] U. Brandt and C. Mielsch, Z. Phys. B **75**, 365 (1989); **79**, 295 (1990); J. K. Freericks, Phys. Rev. B **47**, 9263 (1993).

[17] A. M. Shvaika, Physica C **341-348**, 177 (2000); J. K. Freericks and P. Miller, Phys. Rev. B **62**, 10022 (2000).

[18] Th. Pruschke, D. L. Cox, and M. Jarrell, Phys. Rev. B **47**, 3553 (1993); Europhys. Lett. **21**, 593 (1993).

[19] P. G. J. van Dongen, Phys. Rev. B **45**, 2267 (1992); P. G. J. Van Dongen and C. Leinung, Ann. Phys. (Leipzig) **6**, 45 (1997).

[20] J. K. Freericks, T. P. Devereaux, and R. Bulla (unpublished).